

Waveguide-Based Platform for Large-FOV Imaging of Optically Active Defects in 2D Materials

Evgenii Glushkov,^{*,†} Anna Archetti,[‡] Anton Stroganov,^{†,‡,⊥} Jean Comtet,[†] Mukeshchand Thakur,[†] Vytautas Navikas,[†] Martina Lihter,[†] Juan Francisco Gonzalez Marin,[§] Vitaliy Babenko,^{||} Stephan Hofmann,^{||} Suliana Manley,[‡] and Aleksandra Radenovic^{*,†}

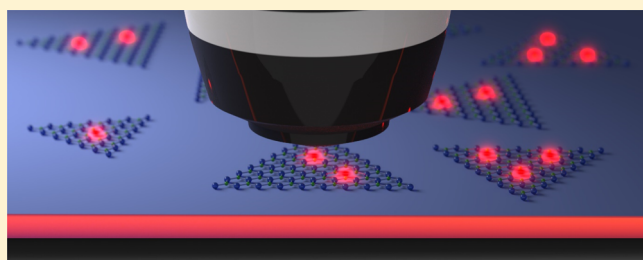
[†]Laboratory of Nanoscale Biology, Institute of Bioengineering, [‡]Laboratory of Experimental Biophysics, Institute of Physics, and [§]Laboratory of Nanoscale Electronics and Structures, Institute of Electrical Engineering and Institute of Materials Science, École Polytechnique Fédérale de Lausanne (EPFL), 1015 Lausanne, Switzerland

^{||}Department of Engineering, University of Cambridge, 9 JJ Thomson Avenue, CB3 0FA Cambridge, United Kingdom

Supporting Information

ABSTRACT: Single-molecule localization microscopy (SMLM) is a powerful tool that is routinely used for nanoscale optical imaging of biological samples. Recently, this approach has been applied to study optically active defects in two-dimensional (2D) materials. Such defects can not only alter the mechanical and optoelectronic properties of 2D materials but also bring new functionalities, which make them a promising platform for integrated nanophotonics and quantum sensing. Most SMLM approaches, however, provide a field of view limited to $\sim 50 \times 50 \mu\text{m}^2$, which is not sufficient for high-throughput characterization of 2D materials. Moreover, the 2D materials themselves pose an additional challenge as their nanometer-scale thickness prevents efficient far-field excitation of optically active defects. To overcome these limitations, we present here a waveguide-based platform for large field-of-view imaging of 2D materials via total internal reflection excitation. We use this platform to perform large-scale characterization of point defects in chemical vapor deposition-grown hexagonal boron nitride on an area of up to $100 \times 1000 \mu\text{m}^2$ and demonstrate its potential for correlative imaging and high-throughput characterization of defects in 2D materials.

KEYWORDS: 2D materials, super-resolution, waveguides, imaging, microscopy, defects



Waveguides have been the workhorse of integrated photonics, serving as the basis for implementing compact passive components such as on-chip splitters, filters, interferometers, resonators, and multiplexers. To add functionality to photonic chips, one further needs to interface waveguides with other materials, which is usually done through coupling with the evanescent field of the waveguide. This method is especially suitable for 2D materials, which due to their minimal thickness down to just a few angstroms are efficiently excited by the evanescent field from the waveguide.¹ This allows for the fabrication of various active components (light-emitting diodes, modulators, photodetectors) from 2D materials on top of the on-chip waveguides.^{2,3} Such devices may utilize not only the optoelectronic properties of the 2D material itself but also those originating from the optically active defects in these materials.^{4–6} The existence of such point emitters has been reported for multiple transition-metal dichalcogenides (TMDCs)^{7–10} at cryogenic temperatures and in hexagonal boron nitride (hBN)¹¹ at room temperature. Recent works have also shown the efficient coupling of the single-photon emission from these defects into the on-chip

waveguides, making them a promising platform for on-chip quantum optics.^{12,13}

Several imaging techniques were demonstrated to be suitable for studying such defects in 2D materials at different scales. Transmission electron microscopy (TEM)^{14,15} can be employed to image single defects over an area of several tens of square nanometers, which is however accompanied by the introduction of new defects during this process due to intense electron-beam irradiation of the studied sample.^{15,16} Near-field techniques, such as scanning tunneling microscopy (STM)¹⁷ and near-field scanning optical microscopy (NSOM),¹⁸ have been also successfully applied to study defects in 2D materials. However, they are all limited by the size of the inspected area (typically, less than several square micrometers) and do not allow for high-throughput characterization of defects due to the time needed for sequential scanning.

While this can be tolerated for certain applications, novel high-throughput inspection methods are crucially needed to rapidly characterize defects in large-area 2D materials.^{19,20} This

Received: July 31, 2019

Published: November 8, 2019

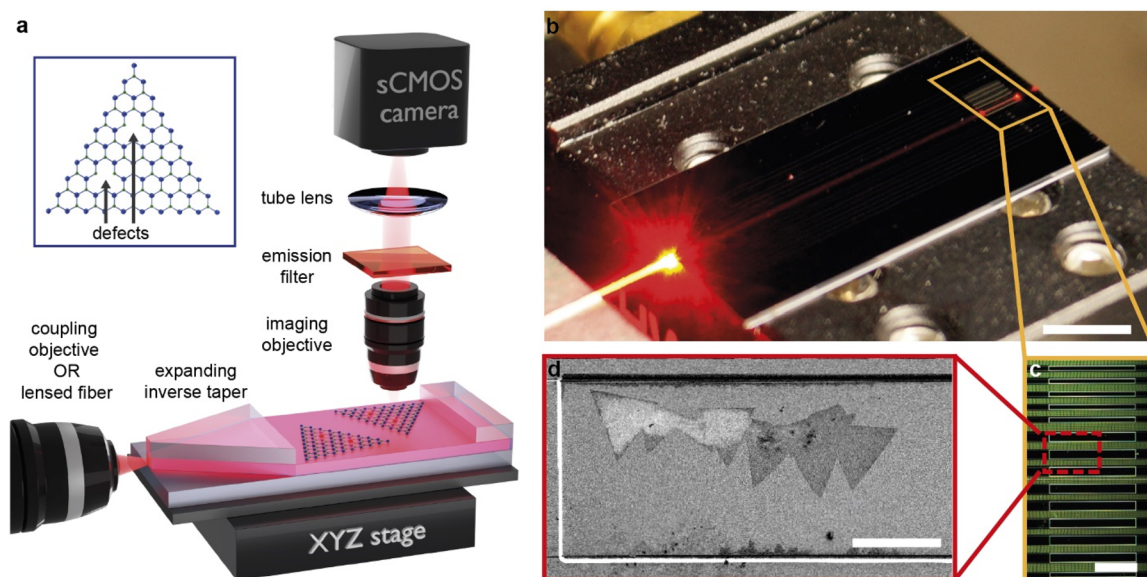


Figure 1. Concept and implementation of the waveguide-based platform for high-throughput photoluminescence characterization and super-resolution imaging of 2D materials. (a) Simplified schematic of the imaging setup, where the laser light is focused onto the tapered entrance of the waveguide from the left and is creating an evanescent field on the surface of the imaging well. This excites the fluorescence in the flakes of 2D materials, which is detected through the imaging column. The inset on the top left shows the atomic structure of a 2D material (e.g., hBN) with defects. (b) Waveguide chip placed on the piezo stage. The red laser is coupled in from the left facet, and its propagation inside the waveguide is visible due to scattering. The scattering signal is significantly higher in the imaging well (outlined in yellow), where the protective top silica cladding is removed. (c) Multiple imaging wells on the same waveguide chip, placed after the expansion taper reached the needed width of the waveguide (25, 50, or 100 μm in the chip shown). (d) An SEM image of transferred CVD-grown hBN flakes inside one of the imaging wells. Scale bar: 5 mm (b), 500 μm (c), 50 μm (d).

is especially important in the context of further wafer-scale integration of 2D materials into standard microelectronics fabrication processes. Here a technique of choice would be wide-field optical microscopy, which uses camera detectors to image the entire field of view in a single shot and thus enables fast characterization of much larger areas than the above-mentioned methods, but provides significantly worse resolution due to the diffraction limit.²¹

The quest to overcome this limit has been central in many areas of biology, which led to the creation of multiple super-resolution microscopy methods, including single-molecule localization microscopy (SMLM).^{22,23} The SMLM technique is based on acquiring a large stack of successive images, each containing sparse switchable fluorophores, which are then localized frame-by-frame. SMLM has become very popular in the biological community, giving rise to the variety of implementations (PALM,²³ STORM,²² SOFI,²⁴ PAINT,^{25,26} etc.) and the creation of ready-to-use commercial super-resolution microscopes by several manufacturers. Recently, however, this technique has found applications in materials science²⁷ and was applied to study optically active defects in 2D materials, by treating them as single emitters and reaching localization precisions below 10 nm.²¹ Therefore, SMLM allows circumventing the trade-off between small-scale, high-resolution TEM images and large-scale, low-resolution optical maps. Moreover, to simultaneously analyze not only spatial but also the spectral distribution of optically active defects in 2D materials, a spectral super-resolution technique was recently applied to study emitters in hBN.²⁸ This allowed their properties to be studied at the ensemble level and revealed multiple populations of fluorescent defects in this material.

Established wide-field super-resolution techniques, however, typically provide a field of view of less than $\sim 50 \times 50 \mu\text{m}^2$,

which is further reduced down to $\sim 20 \times 20 \mu\text{m}^2$ in the total internal fluorescence (TIRF) mode, especially suitable for imaging 2D materials. This mainly happens due to the lack of the illumination uniformity achievable through high-NA objectives²⁹ and is insufficient for high-throughput characterization of 2D materials. To overcome this limitation and simultaneously increase the excitation efficiency of defects in atomically thin 2D materials, one can use integrated waveguides as an imaging platform by utilizing their evanescent field for excitation. This requires a certain rethinking of the geometry of the waveguides, motivated by the high-throughput imaging requirements.

In the integrated photonics community, waveguides are typically meant to be single-mode, which limits their cross-sectional width to a fraction of a micrometer in the visible range. Obviously, this is not sufficient for large-area imaging, where ideally the width of the imaging waveguide should be expanded to tens of micrometers, being limited only by the imaging objective and the chip size of the camera used ($\sim 200 \mu\text{m}$ for commercial detectors at suitable magnifications for single-emitter detection). Naturally, such wide waveguides are inherently multimode, so a slow adiabatic expansion of the single-mode waveguide to reach the required imaging width is needed in order to uniformly excite the photoluminescence (PL) in 2D materials.³⁰

Following this approach, we demonstrate here the use of a waveguide-based imaging platform, recently applied for SMLM bioimaging,^{31,32} for the characterization of defects in 2D materials. The proposed platform decouples the excitation and collection paths, allowing the collection of the PL signal through a high-NA objective while simultaneously exciting the optically active 2D materials over a large area (up to $100 \times 1000 \mu\text{m}^2$) in TIRF mode. This allows for a hundred-fold

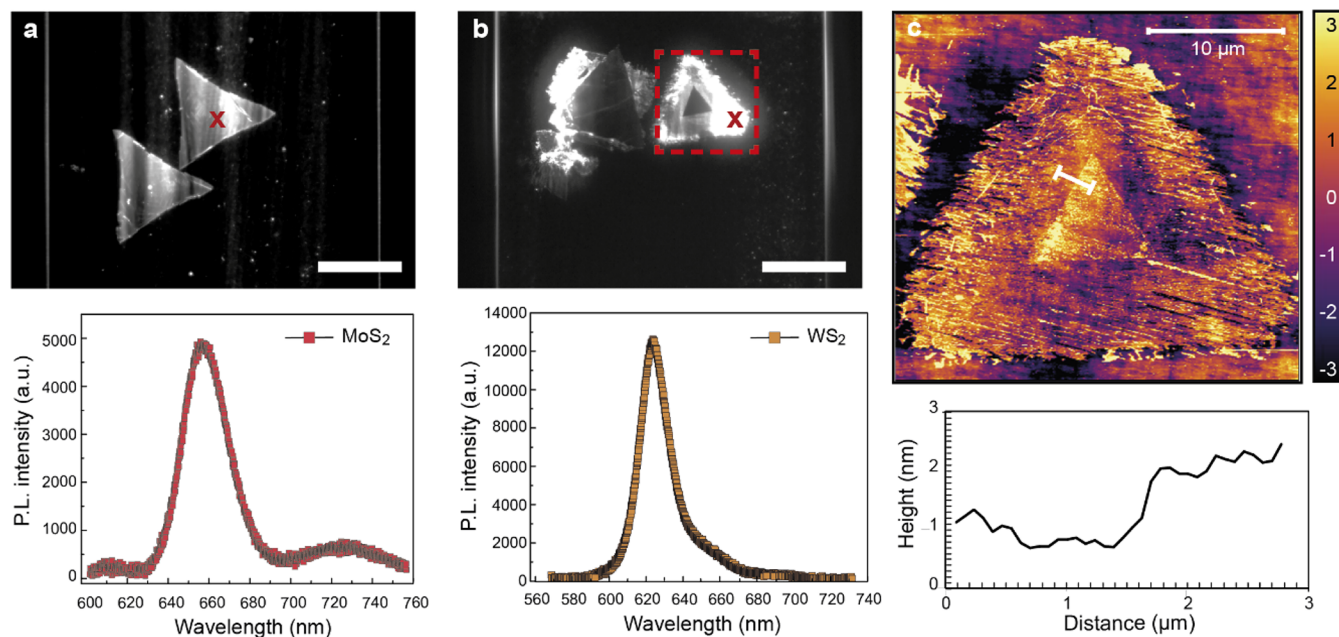


Figure 2. Photoluminescence imaging of 2D semiconductors on waveguides. (a) MoS₂ flakes in the imaging well (top) and the PL spectrum taken at the position of the cross (bottom). (b) WS₂ flakes and their PL spectrum, respectively. (c) AFM scan of dark and bright regions of the WS₂ flake inside the red square and the corresponding averaged line profile (indicated by the width of the line ends), showing a step of ~ 1.5 nm, corresponding to a multilayer material in the center of the flake. The rough borders of the flake are due to the transfer method used. The stripes seen in (a) are also due to the imperfections in the waveguide and transfer residues, which can disturb the mode profile and create some interference. Scale bar: $25 \mu\text{m}$ (a, b).

increase in imaging speed per area, compared to traditional TIRF microscopy or PL mapping, and paves the way toward high-throughput PL characterization and optical inspection of defects in 2D materials.

EXPERIMENTAL SETUP

The central element of the waveguide-based imaging platform is a silicon chip with multiple silicon nitride (Si₃N₄) waveguides buried in the layer of silica cladding (Figure 1a,b). The chip was designed using numerical simulations to have a high coupling efficiency, low losses, and uniform field distribution,³¹ and fabricated using standard microelectronic fabrication processes (see Materials and Methods for details). Particular attention was paid to the input interface of the waveguides, where surface roughness strongly affects the coupling efficiency. To mitigate those losses, we utilized a two-step lithography and etching process, designed to minimize the damage to the input facet.³¹ A further increase in coupling efficiency was achieved by adding an inverted taper coupler (~ 150 nm wide tip) at the beginning of each waveguide, which increases the effective size of the fundamental mode to match the mode size of the input beam. Naturally, the optimal width of the input taper coupler depends on the excitation wavelength and the coupling method used (641 nm laser light and a 50 \times objective, in our case).

The second important requirement for a proper waveguide design is the reduction of transmission losses, maximizing excitation in the imaging area containing the 2D material. Transmission losses were reduced by covering the surface of the waveguides with a protective layer of SiO₂ cladding everywhere except for the small area, the so-called imaging well, where the sample is placed for imaging (see Figure 1c and d for the optical and SEM micrograph of the well,

respectively). Moreover, as discussed above, we preserved the uniform evanescent field in the imaging wells up to $100 \mu\text{m}$ wide, by adiabatically expanding the fundamental mode from the inverted taper coupler with an expansion rate of less than 1% (schematically shown in Figure 1a).

To use the described waveguide chip, we built a simple and cost-effective upright microscope using readily available optomechanical components. As shown in Figure 1, the platform consists of a sample holder to immobilize the waveguide chip, which is placed on top of a 3-axis piezo stage used for alignment, a long-distance coupling objective, an excitation source (561 or 641 nm laser), a high-NA imaging objective, and an sCMOS camera, which collects photoluminescence through exchangeable emission filters in between (see Materials and Methods for details). Alternatively, the waveguide chip can be directly imaged on any existing upright microscope with the addition of a coupling objective or a lensed fiber to couple the laser light into the waveguide chip, which is demonstrated in the SI (Figure S2). The use of a lensed fiber further reduces the cost and complexity of the platform and is especially beneficial when imaging is performed in a vacuum or in a cryogenic environment.

RESULTS AND DISCUSSION

To demonstrate the capabilities of the platform for the investigation of 2D materials, we transferred CVD-grown molybdenum disulfide (MoS₂) and tungsten disulfide (WS₂) flakes—two of the most often used two-dimensional TMDCs—onto the waveguide chips (see Materials and Methods for details). Monolayers of MoS₂ and WS₂ exhibit bright photoluminescence in the visible range (emission maximum at ~ 670 nm for MoS₂ and ~ 630 nm for WS₂),^{33–36} due to the direct band gap of ~ 2 eV, and possess strong excitonic effects,³⁷ which make them especially

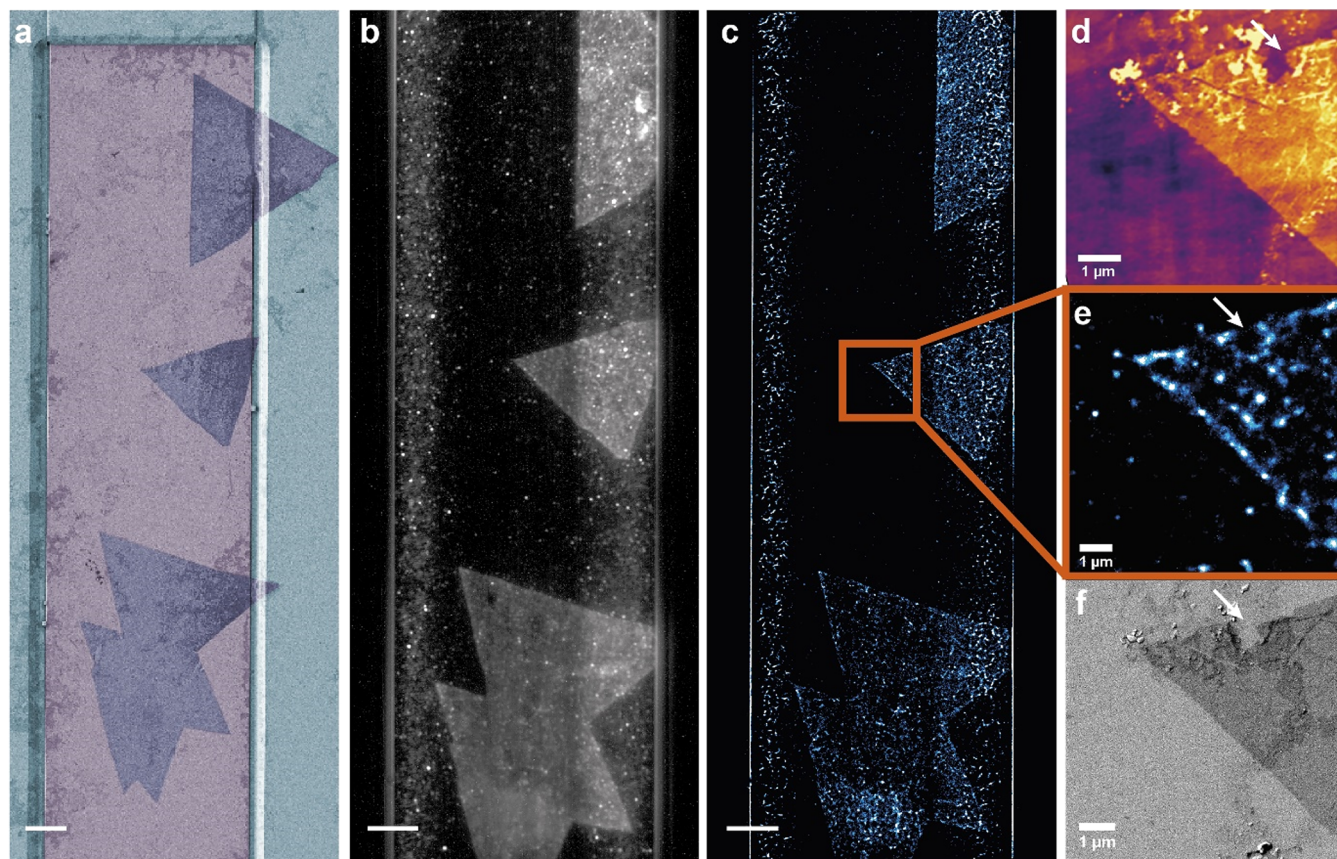


Figure 3. Imaging of optically active defects in hBN on waveguides. (a) An SEM image showing multiple hBN flakes inside a single imaging well, false-colored for clarity. Si_3N_4 waveguide (violet), SiO_2 cladding (light-blue), hBN flakes (dark blue). A larger area is shown, compared to (b) and (c), to demonstrate that only the parts of the flakes inside the imaging well are excited by the evanescent field. (b) Fluorescent image obtained using 641 nm laser excitation (2000 frames, averaged). The observed stripes along the edges of the imaging well are due to residues and inherent impurities in the silica cladding.⁴⁷ The impurities are activated in the high-field intensity regions owing to the curved cross-section of the waveguide.⁴⁸ (c) Reconstructed super-resolved image, obtained from the same stack of 2000 frames. (d–f) Correlative imaging of the ROI, shown by an orange rectangle, with a distinct sub-micrometer feature (AFM, SMLM, SEM). Scale bar is 10 μm (a, c); all images are obtained from a single FOV without any stitching.

attractive for applications in optoelectronics and nanophotonics. Particularly interesting is the ability of such materials to form van der Waals heterostructures with desired functionalities.^{38,39}

Though point defects in two-dimensional TMDCs are usually not optically active at room temperature, they have an effect on the photoluminescence of the material. The PL of TMDCs is normally reduced with the increasing density of defects, thus serving as an indicator of the quality of the 2D material. PL can also be enhanced through defect engineering^{6,40,41} and chemical treatment.^{42,43} In Figure 2 we show the measured wide-field PL signal from MoS_2 (Figure 2a) and WS_2 (Figure 2b) flakes excited by the evanescent field on the surface of waveguide chips, together with their spectra (see Materials and Methods for details). Both materials demonstrate a bright PL signal, compared with the background, even with the excitation laser power as low as 10 mW, measured before the coupling objective. Such power density is orders of magnitude smaller than what is typically needed to illuminate a similar area for PL measurements on conventional wide-field microscopes.

Another advantage of the waveguide platform is the fast acquisition time for PL maps. To obtain the PL maps in Figure 2 ($\sim 100 \times 100 \mu\text{m}^2$) an acquisition time of 100 ms was used, which makes a significant difference in comparison with the

sequential scanning micro-PL, where typical acquisition times for such large areas are on the order of minutes (1000 \times slower). This difference becomes even more significant for larger-area flakes (shown in Figure S3) and continuous films of 2D materials, which are currently under development. An advantage of micro-PL comes from the ability to simultaneously record the spectrum of the photoluminescence, though requiring even longer integration times to achieve a good signal-to-noise ratio. That is why for high-throughput PL analysis spectral characterization capabilities can be further added to the demonstrated waveguide-based platform, e.g., following the approach in ref 28.

Upon closer examination of the PL image of the WS_2 flake (Figure 2b), a pronounced dark triangular region can be observed in the center of each flake, which presumably consists of several atomic layers of the 2D material produced during initial growth at the nucleation center. This is further confirmed by the atomic force microscopy (AFM) scan (Figure 2c), which reveals an averaged line profile with a step of ~ 1.5 nm at the boundary of the dark region. These multilayer structures exhibit much dimmer photoluminescence due to the change from a direct band gap in monolayer WS_2 to an indirect band gap in the multilayer material.⁴⁴ Therefore, the waveguide-based platform can be used as well for a quick

search of multilayer regions on a grown monolayer 2D material, even in case of poor optical contrast.

To investigate the capabilities of the waveguide-based imaging platform for super-resolution defect characterization, we transferred samples of CVD-grown monolayer hBN to the imaging wells on a waveguide chip (see [Materials and Methods](#) for details). As monolayer hBN on top of silicon nitride is barely visible by either bright- and dark-field optical microscopy, we directly proceeded with the investigation of the transferred flakes using fluorescence. Typically, such CVD-grown hBN contains a substantial density of optically active defects, so we could excite them using laser illumination, coupled into the on-chip waveguide, and record the emitted signal with an sCMOS camera. A typical time-averaged wide-field image clearly shows multiple hBN flakes inside an imaging well in [Figure 3b](#).

As was previously reported,²¹ emitters in hBN exhibit pronounced photoswitching between the bright and dark states (blinking) under continuous laser illumination, such that only a fraction of emitters is visible in each of the acquired frames (see [Figure S6](#) for the temporal properties of the studied samples). This enables temporal separation and localization of sparse active emitters with subpixel precision by fitting each of the diffraction-limited luminescence spots with a 2D Gaussian intensity profile and a reconstruction of a super-resolved image by summing up all localizations over a large number of frames (~2000, in our case). The resulting super-resolved image for the acquired image stack, reconstructed using the ThunderSTORM plugin⁴⁵ for ImageJ,⁴⁶ is shown in [Figure 3c](#). Additional reconstructed images of large-area hBN flakes are shown in [Figure S4](#).

As reported in [Figure 3c](#), not only hBN flakes produce the fluorescence, especially in the areas near the edges of the waveguide. Presumably, this parasitic signal is due to polymer residues and inherent impurities in the silica cladding.⁴⁷ These impurities are excited in the regions of the waveguide where the excitation field intensity is high due to the curved cross-section of the waveguide, which was intentionally fabricated with that profile to minimize the scattering losses.⁴⁸ To see the distinction between such emitters in the background versus the ones in hBN flakes, we additionally analyzed their temporal dynamics (SI, [Figure S6c](#)). We also analyzed the spectrum of the observed emission to verify it was coming from the optically active defects in hBN ([Figure S5](#)), which matches the previously published spectra for CVD-grown hBN^{28,49} and is inherently different from the photoluminescence of polymer residues.⁵⁰

To further characterize the transferred 2D material on waveguides, we performed scanning electron microscopy (SEM) ([Figure 3a](#)) and AFM ([Figure 3d](#)) imaging. The strong contrast of hBN on top of silicon nitride in SEM enables relatively quick imaging of sufficiently large areas on the sample to locate all transferred hBN flakes and check for possible polymer residues (visible in areas close to the imaging well in [Figure 2a](#)) mainly coming from poly(methyl methacrylate) (PMMA), used in the transfer process (see [Materials and Methods](#) for details). Higher-resolution SEM imaging, followed by AFM scans of the selected regions-of-interest (ROIs), demonstrates the advantages of the waveguide imaging platform for correlative super-resolution imaging ([Figure 3d–f](#)), thanks to the natural reference frame of each imaging well and waveguide labels, used to navigate the waveguide chip.

While acquired super-resolved images of emitters in hBN provide valuable information about the spatial and temporal distribution of defects in the transferred flakes, for high-throughput characterization of the material it is important to have a certain figure of merit, linked to the properties of the material under study. One such figure of merit could be the average density of optically active defects,²¹ which would be inversely proportional to the quality of the hBN film in comparison to the defect-free crystal. This information can be easily extracted from the localization table ([Figure S7](#)), used to generate the super-resolved image, which allows for an easy integration into automated characterization procedures.

Furthermore, as both the core and the cladding of the waveguide chip are chemically stable, the platform can be readily used to explore the effect of chemical treatments on the optical properties of 2D materials. One example is the treatment with a superacid, such as bis(trifluoromethane)-sulfonamide, which was demonstrated to increase the photoluminescence of 2D materials.⁴² More complicated treatments^{51,52} could be used to heal the defects in CVD-grown 2D materials in an effort to bridge the gap in their quality in comparison to almost defect-free bulk crystals. Moreover, using simple PDMS-based microfluidic channels on top of the waveguide chip, one could image the temporal evolution of such treatments, multiplexed over several waveguides on the same chip.

The waveguide-based platform is also advantageous in the context of further integration with on-chip electronics and microwave circuits. Recent studies have identified certain optically active defects in hBN that demonstrate clear signatures of an optically detected magnetic resonance (ODMR).^{53,54} This discovery opens up a plethora of possibilities for the optical manipulation and readout of spin states in hBN, which is essential for quantum information processing and quantum sensing algorithms. Thus, the addition of microwave and DC lines becomes a necessity and could be easily achievable on the waveguide chip with standard microfabrication techniques.

CONCLUSION

We have designed a novel waveguide-based platform for the investigation of defects in 2D materials and demonstrated its high-throughput capabilities for the characterization of optically active defects in hexagonal boron nitride. We further showed the capabilities of the waveguide-based platform for correlative imaging of defects in 2D materials beyond the diffraction limit. Extending this approach to other types of 2D materials (MoS₂, WS₂), we explored their evanescent-field-driven photoluminescence. Therefore, our approach paves the way toward high-throughput characterization and exploration of defects in various 2D materials both at room temperature and in the cryogenic environment.

MATERIALS AND METHODS

Optical Setup. The home-built microscope has two excitation lasers with a wavelength of 641 nm (CUBE, Coherent) and 561 nm (OBIS, Coherent), which are then coupled into the input facet of the on-chip waveguides using a long-working-distance objective (50× NA 0.55, Mitutoyo). A dipping imaging objective (Nikon CFI Plan 100XC W, 100× magnification, NA 1.1) is mounted from the top with the help of two connected Z-stages, one for long-travel-range vertical

translation (VAP10/M, Thorlabs) and another one for fine micrometer positioning (LNR25D/M, Thorlabs). The same stages hold a set of removable emission filters (ZT405/488/561/640rpc or ET700/75, Chroma). Another mechanically stable system, built with four posts and four rectangular optical breadboards, holds the sCMOS camera (PRIME 95B, Photometrics) and the tube lens (TTL200, 200 mm, Thorlabs). This double mechanical system decouples the vertical motion of the objective from the heavy components and ensures the stability during imaging and quick Z-adjustment.

The waveguide chip is placed in a custom-made holder (3D-printed or micromachined), which is then screwed into an independent double-stage system, in which the first stage (M-401, Newport) enables the FOV adjustment and the second one (MAX311D/M, Thorlabs) is used to align the entrance of the waveguide with the focused laser beam and maximize the coupling efficiency. A more detailed description of the setup can be found in ref 31, together with the complete set of design files.

Chip Fabrication. We fabricated channel waveguides with a rectangular cross-section using Si_3N_4 as the core and SiO_2 as the cladding material on standard silicon wafers, 100 mm in diameter and 525 μm thick. The core material, stoichiometric silicon nitride (Si_3N_4), 150 nm thick, was deposited using a low-pressure chemical vapor deposition (LPCVD) process on top of the 2- μm -thick layer of thermally grown SiO_2 on the silicon substrate. To transfer the layout of the waveguides onto the wafer, we used electron-beam lithography, followed by dry reactive ion etching (RIE). A top cladding layer (2 μm of SiO_2) was deposited by LPCVD (LTO, low temperature oxide). Further photolithography and dry etching steps were used to define the imaging wells. To define the waveguide facets as well as the chip borders, two more steps of photolithography and etching were needed to have a spatial separation of the smooth waveguide entrance from the rough chip border. After the deep etching the wafer was ground from the back until the chips were split apart using the DAG810 automatic surface grinder. The step-by-step fabrication process is schematically shown in the SI (Figure S1) and further detailed in ref 31.

2D Material Growth. CVD-grown hBN material was produced under similar conditions, as described elsewhere.⁵⁵ Briefly, as-received Fe foil (100 μm thick, Goodfellow, 99.8% purity) is cleaned in acetone and IPA and loaded in a customized CVD reactor (base pressure 1×10^{-6} mbar). The substrate was heated to 940 $^\circ\text{C}$ in Ar, followed by annealing in NH_3 (4 mbar). For the growth, NH_3 was used as a carrier gas (1×10^{-2} mbar) and 6×10^{-4} mbar Borazine (HBNH_3) is introduced into the chamber for 30 minutes. The growth was quenched by turning off the heater, allowing a fast cooling rate of about 200 $^\circ\text{C}/\text{min}$ initially.

MoS_2 and WS_2 were grown by the CVD process reported previously.^{20,56}

2D Material Transfer. The as-grown hBN sample was spin-coated with PMMA ($M_r = 495$, 4% solution in anisole, 3000 rpm) and baked for 5 min at 180 $^\circ\text{C}$. The hBN/PMMA layer was lifted-off from the Fe substrate using the electrochemical bubbling method⁵⁷ and transferred onto the waveguide chips. Similarly, MoS_2 and WS_2 materials, grown on sapphire substrates, were spin-coated with PMMA ($M_r = 495$, 4% solution in anisole, 2000 rpm) and baked for 5 min at 180 $^\circ\text{C}$. The MoS_2 /PMMA and WS_2 /PMMA layers were

lifted-off in DI water from the substrate and transferred onto waveguide chips.

The 2D material flakes were precisely aligned into the wells by using a micropositioning stage and a recently reported transfer method.⁵⁸ After the transfer, PMMA was removed by a successive 1 h rinse in hot acetone (3 rinses), hot isopropyl alcohol (1 rinse), and hot DI water (1 rinse). Remaining PMMA contamination is further cleaned by annealing at 400 $^\circ\text{C}$ in an argon (100 sccm) and hydrogen (10 sccm) atmosphere for 8 h.

Imaging and Data Analysis. Imaging was performed using a dipping objective with DI water and an excitation power of the laser varying from 10 to 100 mW. The acquisition time of the sCMOS camera was adjusted to maximize the signal-to-noise without creating overlapping localizations (typically, 50–100 ms). The acquired stacks of thousands of frames were recorded using Micro-Manager⁵⁹ and saved as TIFF files. These files were then imported to the ImageJ software⁴⁶ and analyzed using the Thunderstorm plugin.⁴⁵ The analysis consisted of applying a wavelet filter to each frame and fitting the peak intensities by 2D Gaussian profiles. Only emitters with intensities at least 1.2 times the standard deviation were then assembled into a localization table, which was used to render the super-resolved image (Normalized Gaussian).

Photoluminescence Spectrum. Micro-photoluminescence measurements were performed in air at room temperature. A 50 \times air objective was used to focus the 488 nm laser on a 2 μm spot on the sample to excite the PL, which was collected through the same objective onto the spectrometer (Andor Newton). Laser power was fixed to 300 and 450 μW for MoS_2 and WS_2 , respectively. The acquisition time was set to 60 s for the spectra shown in Figure 2.

AFM and SEM Imaging. The devices were imaged using an atomic force microscope (Asylum Research Cypher) operating in AC mode. The SEM imaging was performed using a ZEISS Leo electron microscope at 1 kV acceleration voltage.

■ ASSOCIATED CONTENT

📄 Supporting Information

The Supporting Information is available free of charge on the ACS Publications website at DOI: 10.1021/acsp Photonics.9b01103.

Schematic representation of the typical process flow used to fabricate the waveguide chips, adding lensed fibers to an existing microscope to use the waveguide platform, large-area MoS_2 flakes on waveguides, hBN flakes on different waveguides, spectra of optically active defects in hBN, temporal properties of the blinking emitters in hBN, and average density of emitters in hBN flakes (PDF)

■ AUTHOR INFORMATION

Corresponding Authors

*E-mail: evgenii.glushkov@epfl.ch.

*E-mail: aleksandra.radenovic@epfl.ch.

ORCID

Martina Lihter: 0000-0003-1859-8453

Stephan Hofmann: 0000-0001-6375-1459

Aleksandra Radenovic: 0000-0001-8194-2785

Present Address

¹LIGENEC SA, Lausanne, Switzerland.

Notes

The authors declare no competing financial interest.

ACKNOWLEDGMENTS

We would like to thank LIGENEC SA and the EPFL Center of Micronanotechnology (CMi) for their help with chip fabrication and the EPFL Laboratory of Quantum Nano-Optics for the assistance with the spectral measurements. E.G. acknowledges the support from the Swiss National Science Foundation through the National Centre of Competence in Research Bio-Inspired Materials. V.B. and S.H. acknowledge funding from the European Union's Horizon 2020 research and innovation program under grant agreement no. 785219.

REFERENCES

- (1) Gonzalez-Marín, J. F.; Unuchek, D.; Watanabe, K.; Taniguchi, T.; Kis, A. MoS₂ photodetectors integrated with photonic circuits. *npj 2D Mater. Appl.* (2019) 3 DOI: 10.1038/s41699-019-0096-4.
- (2) Xia, F.; Wang, H.; Xiao, D.; Dubey, M.; Ramasubramanian, A. Two-dimensional material nanophotonics. *Nat. Photonics* 2014, 8, 899–907.
- (3) Shiue, R.-J.; et al. Active 2D materials for on-chip nanophotonics and quantum optics. *Nanophotonics* 2017, 6, DOI: 10.1515/nanoph-2016-0172.
- (4) Tongay, S.; et al. Defects activated photoluminescence in two-dimensional semiconductors: Interplay between bound, charged, and free excitons. *Sci. Rep.* 2013, 3, 1–5.
- (5) Chow, P. K.; et al. Defect-induced photoluminescence in monolayer semiconducting transition metal dichalcogenides. *ACS Nano* 2015, 9, 1520–1527.
- (6) Nan, H.; et al. Strong photoluminescence enhancement of MoS₂ through defect engineering and oxygen bonding. *ACS Nano* 2014, 8, 5738–5745.
- (7) He, Y.-M.; et al. Single quantum emitters in monolayer semiconductors. *Nat. Nanotechnol.* 2015, 10, 497.
- (8) Chakraborty, C.; Kinnischtzke, L.; Goodfellow, K. M.; Beams, R.; Vamivakas, A. N. Voltage-controlled quantum light from an atomically thin semiconductor. *Nat. Nanotechnol.* 2015, 10, 507.
- (9) Koperski, M.; et al. Single photon emitters in exfoliated WSe₂ structures. *Nat. Nanotechnol.* 2015, 10, 503.
- (10) Srivastava, A.; et al. Optically active quantum dots in monolayer WSe₂. *Nat. Nanotechnol.* 2015, 10, 491.
- (11) Tran, T. T.; Bray, K.; Ford, M. J.; Toth, M.; Aharonovich, I. Quantum emission from hexagonal boron nitride monolayers. *Nat. Nanotechnol.* 2016, 11, 37–41.
- (12) Kim, S.; et al. Integrated on Chip Platform with Quantum Emitters in Layered Materials. *Adv. Opt. Mater.* 2019, 1901132.
- (13) Peyskens, F.; Chakraborty, C.; Muneeb, M.; Van Thourhout, D.; Englund, D. Integration of Single Photon Emitters in 2D Layered Materials with a Silicon Nitride Photonic Chip. *Nat. Commun.* 2019, 10, 1–7.
- (14) Gloter, A.; Urita, K.; Iijima, S.; Suenaga, K.; Hashimoto, A. Direct evidence for atomic defects in graphene layers. *Nature* 2004, 430, 870–873.
- (15) Jin, C.; Lin, F.; Suenaga, K.; Iijima, S. Fabrication of a freestanding boron nitride single layer and its defect assignments. *Phys. Rev. Lett.* 2009, 102, 3–6.
- (16) Kotakoski, J.; Jin, C. H.; Lehtinen, O.; Suenaga, K.; Krashennnikov, A. V. Electron knock-on damage in hexagonal boron nitride monolayers. *Phys. Rev. B: Condens. Matter Mater. Phys.* 2010, 82, 1–4.
- (17) Wong, D.; et al. Characterization and manipulation of individual defects in insulating hexagonal boron nitride using scanning tunnelling microscopy. *Nat. Nanotechnol.* 2015, 10, 949–953.
- (18) Fei, Z.; et al. Electronic and plasmonic phenomena at graphene grain boundaries. *Nat. Nanotechnol.* 2013, 8, 821–825.
- (19) Cun, H.; et al. Centimeter-Sized Single-Orientation Monolayer Hexagonal Boron Nitride With or Without Nanovoids. *Nano Lett.* 2018, 18, 1205–1212.
- (20) Cun, H.; et al. Wafer-scale MOCVD growth of monolayer MoS₂ on sapphire and SiO₂. *Nano Res.* 2019, 12, 2646–2652.
- (21) Feng, J.; et al. Imaging of optically active defects with nanometer resolution. *Nano Lett.* 2018, 18, 1739–1744.
- (22) Rust, M. J.; Bates, M.; Zhuang, X. Sub-diffraction-limit imaging by stochastic optical reconstruction microscopy (STORM). *Nat. Methods* 2006, 3, 793–5.
- (23) Betzig, E.; et al. Imaging Intracellular Fluorescent Proteins at Nanometer Resolution. *Science (Washington, DC, U. S.)* 2006, 313, 1642–1645.
- (24) Dertinger, T.; Colyer, R.; Iyer, G.; Weiss, S.; Enderlein, J. Fast, background-free, 3D super-resolution optical fluctuation imaging (SOFI). *Proc. Natl. Acad. Sci. U. S. A.* 2009, 106, 22287–22292.
- (25) Sharonov, A.; Hochstrasser, R. M. Wide-field subdiffraction imaging by accumulated binding of diffusing probes. *Proc. Natl. Acad. Sci. U. S. A.* 2006, 103, 18911–18916.
- (26) Jungmann, R.; et al. Multiplexed 3D cellular super-resolution imaging with DNA-PAINT and Exchange-PAINT. *Nat. Methods* 2014, 11, 313–318.
- (27) Wöll, D.; Flors, C. Super-resolution Fluorescence Imaging for Materials Science. *Small Methods* 2017, 1, 1700191.
- (28) Comtet, J.; et al. Wide-Field Spectral Super-Resolution Mapping of Optically Active Defects in Hexagonal Boron Nitride. *Nano Lett.* 2019, 19, 2516–2523.
- (29) Fu, Y.; et al. Axial superresolution via multiangle TIRF microscopy with sequential imaging and photobleaching. *Proc. Natl. Acad. Sci. U. S. A.* 2016, 113, 4368–4373.
- (30) Tinguely, J. C.; Helle, O. I.; Ahluwalia, B. S. Silicon nitride waveguide platform for fluorescence microscopy of living cells. *Opt. Express* 2017, 25, 27678–27690.
- (31) Archetti, A.; et al. Waveguide-PAINT offers an open platform for large field-of-view super-resolution imaging. *Nat. Commun.* 2019, 10, 1–9.
- (32) Diekmann, R.; et al. Chip-based wide field-of-view nanoscopy. *Nat. Photonics* 2017, 11, 322–328.
- (33) Mak, K. F.; Lee, C.; Hone, J.; Shan, J.; Heinz, T. F. Atomically thin MoS₂: A new direct-gap semiconductor. *Phys. Rev. Lett.* 2010, 105, 2–5.
- (34) Splendiani, A.; et al. Emerging photoluminescence in monolayer MoS₂. *Nano Lett.* 2010, 10, 1271–1275.
- (35) Cong, C.; et al. Synthesis and optical properties of large-area single-crystalline 2D semiconductor WS₂ monolayer from chemical vapor deposition. *Adv. Opt. Mater.* 2014, 2, 131–136.
- (36) Li, H.; Zhu, X.; Tang, Z. K.; Zhang, X. H. Low-temperature photoluminescence emission of monolayer MoS₂ on diverse substrates grown by CVD. *J. Lumin.* 2018, 199, 210–215.
- (37) Mak, K. F.; Shan, J. Photonics and optoelectronics of 2D semiconductor transition metal dichalcogenides. *Nat. Photonics* 2016, 10, 216–226.
- (38) Unuchek, D.; et al. Room-temperature electrical control of exciton flux in a van der Waals heterostructure. *Nature* 2018, 560, 340–344.
- (39) Ciarrocchi, A.; et al. Polarization switching and electrical control of interlayer excitons in two-dimensional van der Waals heterostructures. *Nat. Photonics* 2019, 13, 131–136.
- (40) Jungwirth, N. R.; et al. Temperature Dependence of Wavelength Selectable Zero-Phonon Emission from Single Defects in Hexagonal Boron Nitride. *Nano Lett.* 2016, 16, 6052–6057.
- (41) Branny, A.; Kumar, S.; Proux, R.; Gerardot, B. D. Deterministic strain-induced arrays of quantum emitters in a two-dimensional semiconductor. *Nat. Commun.* 2017, 8, 1–7.
- (42) Amani, M.; et al. Near-unity photoluminescence quantum yield in MoS₂. *Science (Washington, DC, U. S.)* 2015, 350, 1065–1068.

- (43) Mouri, S.; Miyauchi, Y.; Matsuda, K. Tunable photoluminescence of monolayer MoS₂ via chemical doping. *Nano Lett.* **2013**, *13*, 5944–5948.
- (44) Molas, M. R.; et al. The optical response of monolayer, few-layer and bulk tungsten disulfide. *Nanoscale* **2017**, *9*, 13128–13141.
- (45) Ovesný, M.; Krížek, P.; Borkovec, J.; Švindrych, Z.; Hagen, G. M. ThunderSTORM: a comprehensive ImageJ plug-in for PALM and STORM data analysis and super-resolution imaging. *Bioinformatics* **2014**, *30*, 2389–2390.
- (46) Abramoff, M. D.; et al. Image processing with ImageJ. *Biophotonics Int.* **2004**, *11*, 36–42.
- (47) Rabouw, F. T.; et al. Non-blinking single-photon emitters in silica. *Sci. Rep.* **2016**, *6*, 1–7.
- (48) Pfeiffer, M. H. P.; et al. Ultra-smooth silicon nitride waveguides based on the Damascene reflow process: fabrication and loss origins. *Optica* **2018**, *5*, 884.
- (49) Abidi, I. H.; et al. Selective Defect Formation in Hexagonal Boron Nitride. *Adv. Opt. Mater.* **2019**, *7*.
- (50) Narayana Deepak, K. L.; Rao, V.; Rao, N. Direct Writing in Polymers with Femtosecond Laser Pulses: Physics and Applications. *Laser Pulses - Theory, Technol. Appl.* **2012**, DOI: 10.5772/45854.
- (51) Luo, P.; et al. Doping engineering and functionalization of two-dimensional metal chalcogenides. *Nanoscale Horizons* **2019**, *4*, 26–51.
- (52) Cho, K.; et al. Electrical and Optical Characterization of MoS₂ with Sulfur Vacancy Passivation by Treatment with Alkanethiol Molecules. *ACS Nano* **2015**, *9*, 8044–8053.
- (53) Gottscholl, A.; et al. Room Temperature Initialisation and Readout of Intrinsic Spin Defects in a Van der Waals Crystal. *arXiv* **2019**, 1906.03774.
- (54) Chejanovsky, N.; et al. Single spin resonance in a van der Waals embedded paramagnetic defect. *arXiv* **2019**, 1906.05903.
- (55) Caneva, S.; et al. Controlling Catalyst Bulk Reservoir Effects for Monolayer Hexagonal Boron Nitride CVD. *Nano Lett.* **2016**, *16*, 1250–1261.
- (56) Dumcenco, D.; et al. Large-Area Epitaxial Monolayer MoS₂. *ACS Nano* **2015**, *9*, 4611–4620.
- (57) Gao, L.; et al. Repeated growth and bubbling transfer of graphene with millimetre-size single-crystal grains using platinum. *Nat. Commun.* **2012**, *3*, 697–699.
- (58) Graf, M.; et al. Fabrication and practical applications of molybdenum disulfide nanopores. *Nat. Protoc.* **2019**, *14*, 1130–1168.
- (59) Edelstein, A.; Amodaj, N.; Hoover, K.; Vale, R.; Stuurman, N. Computer Control of Microscopes Using μ Manager. *Curr. Protoc. Mol. Biol.* **2010**, *92*, 14.20.1–14.20.17.